Template-free synthesis and luminescent properties of hollow Ln:YOF (Ln = Eu or Er+Yb) microspheres

E. Martinez-Castro,[a] J. García-Sevillano[b], F. Cussó,[b] M. Ocaña[a]

[a]*Instituto de Ciencia de Materiales de Sevilla (CSIC-US), Americo Vespucio 49, Isla de La Cartuja, 41092 Sevilla, Spain.*

[b]*Dpto. Física de Materiales, C-04, Universidad Autónoma de Madrid, Avda. Francisco Tomás y Valiente, 7, 28049 – Madrid, Spain*

Corresponding Author:

Manuel Ocaña
Postal adddress: Instituto de Ciencia de Materiales de Sevilla (CSIC-US), Americo Vespucio 49, Isla de La Cartuja, 41092 Sevilla, Spain
E-mail address: mjurado@icmse.csic.es
Phone number: (34) 95 448 9533

ABSTRACT

A method for the synthesis of hollow lanthanide doped yttrium oxyfluoride (YOF) spheres in the micrometer size range with cubic structure based on the pyrolysis at 600ºC of liquid aerosols generated from aqueous solutions containing the corresponding rare earth chlorides and trifluoroacetic acid has been developed. This procedure, which has been used for the first time for the synthesis of YFO based materials, is simpler and advantageous when compared with other methods usually employed for the production of hollow spheres since it does not require the use of sacrificial templates. In addition, it is continuous, which is desirable because of practical reasons. The procedure is also suitable for doping the YOF spheres with europium cations resulting in down converting red phosphors when activated with UV light, or for co-doping with both Er^{3+} and Yb^{3+} giving rise to up-converting phosphors, which emit intense red light under near infrared (NIR) irradiation. Because of their optical properties and hollow architecture, the developed materials may find applications in optoelectronic devices and biotechnology.

KEY WORDS: Yttrium oxyfluoride, hollow spheres, europium, erbium, lumincescence

1. Introduction

In the last years, many research efforts have been focussed on the development of well dispersed hollow spherical particles of different luminescent lanthanide (Ln) based compounds [1-12] due to their multifunctional character, which make them suitable for a large variety of applications. Thus, Ln-based luminescent compounds, usually consisting of a host matrix doped with Ln cations, find important applications in lighting [13], display devices [14], solid state lasers [15] and biotechnology (labelling, imaging, drug delivery) [16,17], to mention a few. The main advantages of this kind of luminescent materials over other well known phosphors (quantum dots, organic dyes) are their high chemical and thermal resistance, photostability, low toxicity and their versatility, since they may be designed as down-conversion (DC) phosphors (when doped with Eu, Tb, Sm, Dy), which usually are excited by ultraviolet (UV) light, or as up-conversion (UC) phosphors (when co-doping with Yb and mainly Er or Tm) [16]. These UC phosphors, which show visible emission after excitation with infrared (IR) radiation, are of particular interest for bioapplications when compared with DC phosphors since, contrary to UV radiation, IR light does not cause photodamage to living organisms and penetrates deeply in tissues [17]. The hollow architecture confers to these materials low effective densities and a high encapsulation ability, which are very important for some of the above applications. For example, the combination of a hollow structure and luminescent properties enables the possibility of using these materials for simultaneous drug delivery and cells tracking by fluorescence imaging [18]. For optoelectronic applications, the hollow structure could also reduce the usage of the raw materials and eliminate the cost in commercial production, because most contribution to the photoluminescence comes from the phosphor surface [10].

Hitherto, most reports dealing with luminescent Ln-based systems consisting of hollow spheres, involve the use oxidic (oxides [4,6,7,10], phosphates [1.3], vanadates) [9,11,12] or fluoride [2,5,8] hosts. The former have the advantages of their high chemical and thermal stability, whereas fluorides are more preferred than oxides from the optical point of view, since the former have lower vibrational energies and consequently, the quenching of the exited state of the Ln cations through multiphonon relaxation is minimised, resulting in a higher quantum efficiency of luminescence [17,19]. Less attention has been paid to Ln oxyfluorides (LnOF), which have been suggested as excellent hosts since they combine the main advantages of oxides with those of fluorides [20]. In fact, to best of our knowledge, only a single report on the synthesis of Eu:YOF hollow spheres can be found, which resulted in a rather heterogeneous system consisting of aggregated hollow structures along with some other irregular particles [21].

The most usual procedures for the synthesis of hollow architectures are based on the use of sacrificial (polymers [22], silica [23], carbon [24], among others) templates, which have to be previously fabricated and finally removed through a multistep and time-consuming process. Therefore, the availability of template-free methods for the synthesis of hollow particles would be highly desirable. Spray pyrolysis is a well established procedure for the synthesis of dense spherical particles of different inorganic materials, which is based on the thermal decomposition of liquid aerosols generated from solutions of the corresponding metal cations [25,26]. However, it has been shown than under certain experimental conditions (mainly nature of precursors and temperatures), it is possible that the precipitation of precursors during the drying of the aerosol droplets takes place preferentially at the droplet surface, thus leading to the production of hollow spheres [25-26]. This aerosol procedure is of particular interest

since it is continuous and involves a higher yield than other solution based procedures, which is highly desirable because of practical reasons.

In this paper, we report for the first time a template-free simple method for the synthesis of luminescent hollow Ln-doped YOF spheres based on the pyrolysis at 600ºC of liquid aerosols generated from aqueous solutions of rare-earth (RE) chlorides and trifluoroacetic acid (TFA). It has been shown by Mosiadz el al. [27], who recently studied the thermal decomposition of yttrium trifluoroacetate under different atmospheres (Ar or air), that the trifluoroacetate species decompose on heating at ~275ºC, resulting in yttrium fluoride (YF_3). These authors also reported that the presence of water induces the hydrolysis of YF_3 to yttrium oxyfluorides (YOF and/or $Y_7O_6F_9$) when the heating temperature was raised above 600ºC [27]. The use of this fluoride source is essential to avoid instantaneous precipitation of rare earth fluoride (REF_3) in the starting solutions, which would be produced when using other inorganic fluoride salts. As proof of concept, the here developed procedure is first illustrated for the preparation of Eu^{3+} doped samples, which shows DC luminescence. In this case, the effects of Eu content on theirs optical properties are also analyzed in order to find the optimum system for their potential applications in optical imaging. The suitability of the reported method for the synthesis of UC phosphors is also demonstrated by using both, Er^{3+} and Yb^{3+}, as doping cations. It must be mentioned than whereas the spray pyrolysis procedure has been widely used for the synthesis of different oxidic hollow particles, this is the first report showing its suitability for the synthesis of fluoride containing Ln based compounds.

2. Experimental section

2.1.Reagents.

Yttrium chloride ($YCl_3 \cdot 6H_2O$, Aldrich, 99.9%), europium chloride ($EuCl_3 \cdot 6H_2O$, Aldrich, 99.9%), ytterbium chloride ($YbCl_3 \cdot 6H_2O$, Aldrich, 99.9%) and erbium chloride ($ErCl_3 \cdot 6H_2O$, Aldrich, 99.9%) were used as RE precursors, whereas trifluroroacetic acid (CF_3-COOH, Aldrich, >99%) was used as fluoride source. All chemical were used as received.

2.2.Particles synthesis.

The spherical hollow particles of the selected RE-based YOF were synthesized by pyrolysis of liquid aerosols in the apparatus schematized in Fig. 1, according to the following procedure. Aqueous solutions were first prepared by dissolving proper amounts of the RE precursors. The total RE concentration in these solutions was kept at 0.2 mol dm^{-3}. For the down conversion system, the Ln/Y (Ln = Eu or Er +Yb) molar ratio was varied in the 2-16% range whereas for the up-conversion sample. the Er/Y and the Y/Yb ratios were fixed at 2 and 10%, respectively. An aliquot of trifluoroacetic acid was then admixed so that its final concentration was 0.2 mol $dm^{-3}$and these starting solutions were nebulized using a glass nozzle and air at constant pressure (0.5 kg cm^{-2}) as a carrier gas. The resulting aerosols were introduced into an expansion chamber and transported through two consecutive furnaces kept at 250 and 600ºC, respectively, in which, the liquid droplets were dried and thermally decomposed. The resulting particles were finally collected in a glass filter with a very high efficiency.

2.3. Characterization.

Particle shape was examined by transmission (TEM, Philips 200CM) and scanning (SEM-FEG, Model S4800, Hitachi) electron microscopy. Particle size distributions were obtained by laser diffraction (Malvern Mastersizer). The high angle angular dark field-scanning transmission electron microscopy (HAADF-STEM) image and the EDX (energy-dispersive X-ray spectroscopy) line profile were performed using a FEI FEG

(filed emission gun) -TEM Tecnai G2 F30 S-Twin, equipped with a HAADF detector from Fischione Instruments and a SDD X-Max energy-dispersive x-ray spectrometer (EDXS) detector from Oxford Instruments. The quantitative composition of the samples was analyzed by inductively coupled plasma atomic emission spectroscopy (ICP-AES, Horiba Jobin Yvon, Ultima 2).

The crystalline structure of the prepared samples was assessed from their X-ray diffraction pattern (XRD, Panalytical, X´Pert Prowith an X-Celerator detector) collected at intervals of 0.03° (2θ) and an accumulation time of 3000 s. Crystallite size was obtained from the XRD reflection at ~32.9º (2θ), using the Scherrer formula. Unit cell parameters were determined from the XRD data (collected at intervals of 0.02° (2θ) for an accumulation time for interval of 4000 s) by Rietveld refinement using the Xpert HighScore Plus software. The starting parameters were taken from [28].

The infrared spectra (FTIR) of the nanophosphors diluted in KBr pellets were recorded in a Jasco FT/IR-6200 Fourier transform spectrometer. Thermogravimetric analyses (TGA) were performed in air at a heating rate of 10°C min^{-1}, using a Q600 TA Instrument.

BET specific surface area was measured in a Micromeritics ASAP 2010 apparatus with nitrogen at 77K. Before measurements, the samples were heated under vacuum at 150ºC for two hours.

The excitation and emission spectra of the Eu-doped nanophosphors dispersed in water (0.5 mg cm^{-3}) were recorded in a Horiba Jobin-Yvon Fluorolog3 spectrofluorometer operating in the front face mode. Lifetime measurements were obtained under pulsed excitation at 532 and 266 nm by using the second and fourth harmonics of a neodymium doped yttrium aluminium garnet (Nd:YAG) laser (Spectra Physics model DCR 2/2A 3378), respectively, with a pulse width of 10 ns and a repetition rate of 10 Hz. The

fluorescence was analyzed through an ARC monochromator model SpectraPro 500-i and then detected synchronously with an EMI-9558QB photomultiplier and recorded by a Tektronix TDS420 digital oscilloscope. The UC spectra of the powdered samples were obtained using a Ti: sapphire laser (model 3900S Spectra Physics) operating at ~ 980 nm to excite the Yb^{3+} ions with different excitation powers. Er^{3+} luminescence was detected by the EMI-9558QB photomultiplier tube, in the visible range, or by a Judson InGaAs photodiode in the IR spectral range.

The photographs showing the luminescence of the Eu-doped and Er, Yb codoped phosphors were taken under illumination with ultraviolet radiation (λ= 254 nm), filtered from a Hg discharge a lamp, and under irradiation with the Ti-saphire laser (λ=980 nm), respectively.

3. Results and discussion

3.1. Synthesis and characterization

Irrespective of their europium content, all synthesised Eu-doped samples showed similar morphological characteristics, which are illustrated here for the sample having a 12% Eu (Eu/Y mol ratio) chosen as a representative example. As observed in Fig. 2, this sample was mostly composed of spherical particles as expected from the spray pyrolysis technique. The volumetric size distribution obtained for these spheres (Fig. 3) was bimodal, showing two modes centred at and 3.6 and 0.35 μm. Such a broad size distribution is usually observed when using a pneumatic nebuliser, which requires a high gas pressure, thus inducing collisions among the aerosol droplets, and therefore, their coalescence into bigger entities [29,30]. The observation of the sample under the TEM microscope (Fig. 2, bottom) suggests that the spheres were hollow, since the contrast of the areas close to the particles surface is darker than that of their inner part.

Such suggestion was further confirmed by using the HAADF-STEM imaging techniques where the signal intensity is proportional to ($Z^{3/2}$ x t), where Z is the atomic number and t is sample thickness. The HAADF-STEM image taken for a single sphere is shown in Fig. 4a, whereas the analysis of the intensity profile of this image along the scanned line is displayed in Fig. 4b, which clearly shows a much higher intensity (higher density) at the particle outer shell. The Eu, Y and F elemental distribution obtained measuring the EDX line-profile spectra along the scanned line, follow the same profile than the intensity of the HAADF signal (Fig. 4c), indicating that these elements are accumulated at the surface of the sphere, thus confirming the hollow morphology. According to these analyses, the shell thickness was ~75 nm.

As a consequence of their hollow nature, a rather high specific BET surface area (10 m^2 g^{-1}) was obtained for this sample from the measured N_2 adsorption isotherm (Fig. 5), which is typical (type II) of non-porous or macroporous systems.

The FTIR spectrum recorded for this sample (Fig. 6) indicates the complete decomposition of precursors after the pyrolysis process since it only displays two absorption at 3400 and 1650 cm^{-1} due to absorbed water, very weak features at 1400-1300 cm^{-1}, which might be due to adsorbed carbonate ions coming from atmospheric CO_2, and lattice vibrations at <700 cm^{-1}, which are very similar to those previously observed for the YOF phase [31]. In agreement with this observation, the XRD pattern of the sample (Fig. 7, top) was consistent with the ICDD file for cubic YOF (01-075-0051), although the reflections appeared shifted to lower 2θ values, probably due to the substitution of Y^{3+} (ionic radius in eightfold coordination = 1.02 Å) by Eu^{3+} cations (ionic radius in eightfold coordination = 1.07 Å) in the YOF lattice. Similar XRD patterns were obtained for the other Eu-doped samples, which according to the ICP analyses presented Eu/Y mol ratio values close to the nominal ones (Table 1), indicating

the stoichiometric incorporation of Eu to the YOF matrix. The analysis of the unit cell parameters (Table 1) of these samples gives additional information on this matter. Thus, when the unit cell volume was plotted as a function of the Eu content (Fig. 7, bottom) a linear increase of such magnitude was observed for doping levels in the 2-12% range, confirming the incorporation of the whole amount of Eu added to the Eu:YOF structure. However, the further increase of the Eu content up to 16% resulted in an increase of the unit cell volume lower than expected (Fig. 7, bottom), which seems to suggest the segregation of some Eu cations from the YOF lattice at such doping levels. It should be also noted that the size of the crystalline domains estimated for the hollow spheres was ~20 nm, irrespective of the Eu doping level, which is clearly lower than the shell thickness determined from EDX line-profile analysis (~75 nm). This finding seems to indicate that the hollow spheres are polycrystalline.

When Er^{3+} (2%) and Yb^{3+} (10%) were used as doping cations instead of Eu^{3+}, hollow spherical particles quite similar to those shown in Fig. 2 were obtained. The XRD pattern of this sample (Fig. 8) was also consistent with cubic YOF (ICDD file 01-075-0051). The successful incorporation of the doping cations to the spheres was confirmed by ICP analyses which gave an Er and Yb content similar to the nominal values (Table 1), as well as by their unit cell parameters, which were lower than those corresponding to the Eu-doped samples (Table 1), as expected from the lower values of ionic radius of Er^{3+} (1.0 Å) and Yb^{3+} (0.98 Å), when compared with that of Eu^{3+} (1.07 Å).

3.2. Luminescence properties

3.2.1. Down-converting Eu-doped YOF phosphors.

The emission spectra recorded for the Eu:YOF nanophosphors using an excitation wavelength of 395 nm (direct excitation of the Eu^{3+} ground state to a higher level of the 4f-manifold ($^7F_0$-$^5L_6$) [31] are shown in Fig. 9. As observed, all spectra displayed the

emission bands due to the $^5D_0$- ^7F_J (J =0, 1, 2, 3 and 4) electronic transitions expected for the Eu^{3+}cations in the YOF matrix, having the most intense emissions in the 580-620 nm region [31-33]. It is important to mention that the relative intensity of the $^5D_0$-$^7F_2$ emission band was much higher than that associated to the $^5D_0$-$^7F_1$ transition, which has been previously observed for this system and attributed to the localization of the Eu^{3+} cations in crystallographic sites without inversion centre [31]. In Fig. 9, it can be also observed that the intensity of the emission bands increased as increasing the Eu doping level up to a 12% due an increase of the emission centres, and then decreased for higher (16%) Eu content, suggesting the presence of the well known concentration quenching effect at such Eu content. To gain further information on this luminescent behaviour, lifetimes of $^5D_0$ Eu manifold have been measured under the excitation provided by the second harmonic of a pulsed Nd:YAG laser (λ_{exc} = 532 nm). This excitation efficiently populates the $^5D_1$ multiplet ($^7F_0 \rightarrow {}^5D_1$ transition) which then populates the $^5D_0$ state via non-radiative relaxation [34] from where the different visible emissions originate. It has been verified that the emission spectra under this excitation are coincident with those obtained after 395 nm excitation shown in Fig. 9. The normalized temporal decays of the $^5D_0$ level, measured at λ_{em} = 612 nm ($^5D_0 \rightarrow {}^7F_2$ transition), for different Eu concentrations are shown in Fig. 10. After an initial rise, that corresponds to the filling of the $^5D_0$ emitting level from the upper $^5D_1$ level, the luminescence decays follow, in all cases, a mono-exponential time dependence:

$$I(t) = I_0 \exp(-t/\tau)$$

The emission lifetimes (τ) obtained for the different Eu concentrations are shown in Table 1. As observed, the emission lifetime remained almost constant (2.2 ± 0.2 ms) in the 2-12% Eu content range and then decreased (1.4 ± 0.2 ms) at higher Eu doping levels (16%). It has been also checked that similar values of (τ) are obtained when the

decays are measured in the other luminescence bands originated from the $^5D_0$ Eu level (data not shown). Consequently, it can be concluded that concentration quenching is present in our samples for doping levels above 12%. Therefore, the most efficient among the here obtained Eu:YOF phosphors showing the most intense emissions is that containing a 12 % of Eu (mole ratio).

The luminescence quantum yield can be estimated from the comparison of the different luminescence emissions from the $^5D_0$ multiplet, particularly comparing the intensities of the electric-dipole allowed transitions ($^5D_0 \rightarrow {}^7F_J$; J =2,4) with that associated to the $^5D_0 \rightarrow {}^7F_1$ transition ($\lambda_{emi} \sim 590$ nm) that corresponds to a purely magnetic dipole character. The transition $^5D_0 \rightarrow {}^7F_6$ is not considered, because it is not observed in the luminescence spectra, in accordance with the results in other Eu^{3+} – doped hosts [35-37].

The dipole strength of the magnetic-dipole allowed the $^5D_0 \rightarrow {}^7F_1$ transition is practically independent of the ion's surroundings, so that the transition rate can be calculated incorporating the corresponding local field correction, provided that the refractive index of the material is known. Considering that this index is not expected to change appreciably for our cubic YOF phase when compared with that of the rhombohedral one, we can take then the value of the radiative rate for the dipolar magnetic transition ($A_{0\text{-}1} \approx 50\ s^{-1}$) reported for the latter [32] to calculate its value for those of electric dipole character ($A_{0\text{-}2}$, $A_{0\text{-}4}$) corresponding to our samples.

The ratio between radiative rates of the electric dipole transitions ($A_{0\text{-}2,4}$) and the dipolar magnetic one ($A_{0\text{-}1}$) are related to the corresponding ratios of the intensities of their respective luminescence bands as:

$$\boldsymbol{A_{0-2,4} = A_{0-1} \times \left(\frac{I_{0-2,4} \times h\nu_{0-1}}{I_{0-1} \times h\nu_{0-2,4}} \right)} \quad (2)$$

where $I_{0\text{-}J}$ is the integrated emission intensity and $\nu_{0\text{-}J}$ the center frequency of the $^5D_0 \rightarrow {}^7F_J$ transition (J = 1,2,4), that can be evaluated experimentally from the luminescence spectra. The calculated transition rates are found to be independent of Eu^{3+} concentration, within a 5 % standard deviation from the mean values: A_{02} = 342 s^{-1} and A_{04} = 58 s^{-1}.

The corresponding total radiative probability of the $^5D_0$ level can be now calculated as:

$$\boldsymbol{A_{rad} = A_{md} + A_{ed} = A_{0-1} + \sum_{J=2,4} A_{0-J} = 450\ s^{-1}} \tag{3}$$

which corresponds to a radiative lifetime of τ_{rad} = 2.2 ms.

The luminescence quantum yield (QY) is obtained from the ratio between the radiative transition probability (A_{rad}) and the total transition probability (radiative plus non-radiative, A_{nr}), which is given by the reciprocal of the experimental lifetime (τ_{exp}):

$$\boldsymbol{QY = \frac{A_{rad}}{A_{rad} + A_{no-rad}} = \frac{\tau_{exp}}{\tau_{rad}} = A_{rad}\tau_{exp}} \tag{4}$$

The calculated values for the different doping levels are included in Table 1. It can be observed that the efficiency remains above QY = 90 % for doping levels up to $[Eu^{3+}] \leq$ 12 % and decreases to QY = 64 % for the highest Eu content (16 %).

It is also possible to calculate the Judd-Ofelt intensity parameters (Ω_λ, λ = 2,4), which are related to the radiative emission rates as:

$$\boldsymbol{A_{0-2,4} = \frac{64\pi^4 \nu_{0-2,4}^3}{3hc^3} \frac{e^2}{4\pi\varepsilon_0} \chi_{ed} \sum_{\lambda=2,4,6} \Omega_\lambda \left| \left\langle {}^5D_0 \left| U^{(\lambda)} \right| {}^7F_{2,} \right\rangle \right|^2} \tag{5}$$

where χ_{ed} is the local field correction factor and $\left| \left\langle {}^5D_0 \left| U^{(\lambda)} \right| {}^7F_{2,4} \right\rangle \right|^2$ are the squared reduced matrix elements of the transition $^5D_0 \rightarrow {}^7F_{2,4}$, being $\boldsymbol{\left| \left\langle {}^5D_0 \left| U^{(2)} \right| {}^7F_2 \right\rangle \right|^2 = 0.0032}$

and $\left|\left\langle {}^5\boldsymbol{D_0}\left|\boldsymbol{U}^{(4)}\right|{}^7\boldsymbol{F_4}\right\rangle\right|^2 = \mathbf{0.0023}$ the only nonzero elements [37]. From the experimentally determined transition probabilities given above and the reported values of the local field correction factor, χ_{ed} = 4,98 [32]), we obtain $\Omega_2 = 7.0 \times 10^{-24}$ m^2 and $\Omega_4 = 2.4 \times 10^{-24}$ m^2, which are slightly higher than the values reported for other YOF phases [32].

It must be noticed the similar analyses for the Eu:YOF system have been addressed only in a few previous works, which were conducted on phosphors with orthorhombic structure and that the obtained QY values were much lower (~~50%) [31,32] than those measured for our samples. Therefore, the here developed Eu:YOF hollow spheres show the higher luminescence efficiency so far reported, which might be related to their different crystalline structure (cubic), among other factors (purity, crystallinity). In addition, concentration quenching has been found to be present in our samples at much higher levels of Eu doping (16%) than in these previous works (5%), which is advantageous from the practical point of view since, as a consequence, phosphors with higher emissions intensity can be obtained.

Additional information on the luminescent properties of the Eu doped nanophophors was obtained from the excitation spectrum recorded by monitoring the most intense Eu^{3+} emission (618 nm), which is illustrated for the case of most efficient sample ($Eu_{0.12}Y_{0.88}OF$) (Fig. 11, top). This spectrum displayed the excitation bands corresponding to the direct excitation of the Eu^{3+} ground state to higher levels of the 4f-manifold (between 270 and 400 nm) [33] along with a strong band whose maximum lyes at beyond the wavelength range of our equipment (<250 nm). A similar band has been previously for Eu:YOF samples and attributed to a Eu-O charge transfer transition (CTB) caused by electron delocalization from the filled 2p shell of O^{2-} to the partially filled 4f shell of Eu^{3+}[33]. As observed in Fig. 11 (bottom), the intensity of the Eu^{3+}

emissions was considerably higher when exciting through such CTB band (250 nm) than by direct excitation of the Eu^{3+} electronic levels (λ_{ex} = 395 nm). It was also found that the lifetime values obtained for all transition originated from the $^5D_0$ Eu level under excitation into the CTB (266 nm) were very similar (Table 1) to those obtained for the direct excitation of the Eu cations (λ_{ex} = 532 nm). These results indicate that the former excitation path, which gives rise to a strong red emission (Fig. 11, inset), is more favourable for the potential applications of these phosphors.

3.2.2. Up-converting Er,Yb-codoped YOF phosphors.

After excitation of the Yb cations at $\lambda_{ex} \approx$ 980 nm ($^2F_{7/2} \rightarrow {}^2F_{5/2}$ ground state absorption), different energy transfer processes (ET 1-3) lead to excitation of different excited state levels of Er ions, as it is sketched in Fig. 12. A first resonant transfer process (ET-1) occurs between the $^2F_{5/2}$ Yb level and $^4I_{11/2}$ Er level ($^2F_{5/2} \rightarrow {}^2F_{7/2}$ (Yb^{3+}): $4I_{15/2} \rightarrow {}^4I_{11/2}$ (Er^{3+})), that subsequently populates the lower lying $^4I_{13/2}$ Er multiplet. Consequently, two near IR DC emissions at 980 nm and 1.5 μm appear in the emission spectra of our Er(2%), Yb(10%) codoped YOF sample, as shown in Fig. 13 (a). The first one originates from the spectrally overlapped Yb and Er transitions ($^2F_{5/2} \rightarrow {}^2F_{7/2}$ and $^4I_{11/2} \rightarrow {}^4I_{15/2}$, respectively) while the last one corresponds to the Er ($^4I_{13/2} \rightarrow {}^4I_{15/2}$) transition.

Energy transfer up-conversion is also produced after Yb^{3+} excitation, giving rise to two emissions in the visible spectral range, shown in Figure 13b. The red one (630 nm < λ_{em} < 700 nm) corresponds to the $^4F_{9/2} \rightarrow {}^4I_{15/2}$ transition while the green one (500 < λ_{em} < 570 nm) is associated to emission from the thermally coupled $^2H_{11/2}$ & $^4S_{3/2}$ multiplets ($^2H_{11/2}$ & $^4S_{3/2} \rightarrow {}^4I_{15/2}$). The corresponding energy transfer schemes, also indicated in Fig. 12, are ET-2: ($^2F_{5/2} \rightarrow {}^2F_{7/2}$ (Yb^{3+}): $4I_{13/2} \rightarrow {}^4F_{9/2}$ (Er^{3+})), reaching the $^4F_{9/2}$ red

emitting level and ET-3: ($^2F_{5/2} \rightarrow {}^2F_{7/2}$ (Yb^{3+}): $4I_{11/2} \rightarrow {}^4F_{7/2}$ (Er^{3+})), reaching the $^4F_{7/2}$ level and then, by non-radiative relaxation, the $^2H_{11/2}$ & $^4S_{3/2}$ manifold.

The power dependence of the up-converted emissions are presented, in a double logarithmic plot in Fig. 14. As it can be observed, both the green and red emissions exhibit a quadratic dependence indicating that, in both cases, the emission of an up-converted photon involves the absorption of two excitation photons, in accordance with the need of two energy transfer processes in order to reach the visible emitting Er multiplets, as mentioned above.

Let us finally indicate that the green to red emission ratio of Er^{3+} ions can be modified by different factors, such as the nature of the host material, dopant concentration, particle size or excitation power [20, 38-48]. In the case of the YOF microspheres here presented, it is apparent that the red emission dominates, in agreement with previous observations [20,31,43], giving the material a bright red appearance as shown in the inset of Figure 13b. It is important to mention that this feature gives to this material an important advantage for imaging biomedical applications when compared with other Yb^{3+} /Er^{3+} doped materials which, in many cases, use hosts were the green emission dominates [38,41], considering the substantially reduced absorbance of biological tissues in the red spectral range in comparison to the green portion of the spectra, thus increasing then the penetration depth [44].

4. Conclusions

Lanthanide doped yttrium oxyfluoride (YOF) hollow spheres in the micrometer size range with cubic structure have been synthesized by pyrolysis at 600ºC of liquid aerosols generated from aqueous solutions containing the corresponding rare earth chlorides and trifluoroacetic acid. This procedure, which has been used for the first

time for the synthesis of YFO based materials, is simpler and advantageous when compared with other methods usually employed for the production of hollow spheres since it does not require the use of sacrificial templates. In addition, it is continuous which is desirable because of practical reasons. When doped these spheres with Eu^{3+} cations down converting red phosphors resulted upon UV excitation showing a concentration quenching effect at much higher Eu doping levels than other previously reported samples of the same nature, which involves improved luminescent properties. Up-converting hollow phosphors have been also prepared by codoping the with Er^{3+} and Yb^{3} cations, which emit bright purer red light after NIR excitation than other commonly used matrices. Because of their optical properties and hollow architecture, the developed materials may find applications in optoelectronic devices and biotechnology.

Acknowledgements

This work has been supported by Junta de Andalucía (Grant FQM6090), the Spanish CICYT (Grants MAT2011-23593 and MAT2012-34919**),** CSIC (201460E005) and European Union (CT-REGPOT-2011-1-285895 AL-NANOFUNC).

References

[1] M. Guan, F. Tao, J. Sun, Z. Xu, Facile preparation method for rare earth phosphate hollow spheres and their photoluminescence properties, Langmuir 24 (2008) 8280-8283

[2] F. Zhang, Y. Shi, X. Sun, D. Zhao, G. D. Stucky. Formation of Hollow Upconversion Rare-Earth Fluoride Nanospheres: Nanoscale Kirkendall Effect During Ion Exchange. Chem. Mater. 21 (2009) 5237–5243

[3] L. Zhang, G. Jia, H. You, K. Liu, M. Yang, Y. Song, Y. Zheng, Y. Huang, N. Guo, H. Zhang. Sacrificial Template Method for Fabrication of Submicrometer-Sized $YPO_4:Eu^{3+}$ Hierarchical Hollow Spheres Inorg. Chem. 49 (2010) 3305–3309

[4] G. Jia, H. You, K. Liu, Y. Zheng, N. Guo, H. Zhang. Highly Uniform Gd_2O_3 Hollow Microspheres: Template-Directed Synthesis and Luminescence Properties. Langmuir 26 (2010) 5122–5128

[5] J. Shan, N. Yao, Y. Ju. Phase transition induced formation of hollow structures in colloidal lanthanide-doped $NaYF_4$ nanocrystals. J. Nanopart. Res. 12 (2010) 1429–1438

[6] F. He, P. Yang, D. Wang, C. Li, N. Niu, S. Gai, M. Zhang. Preparation and Up-conversion Luminescence of Hollow La_2O_3:Ln (Ln = Yb/Er, Yb/Ho) Microspheres. Langmuir 27 (2011) 5616–5623

[7] Z. Xu, Y. Gao, T. Liu, L. Wang, S. Biana, J. Lin. General and facile method to fabricate uniform $Y_2O_3:Ln^{3+}$ (Ln^{3+} = Eu^{3+}, Tb^{3+}) hollow microspheres using polystyrene spheres as templates. J. Mater. Chem. 22 (2012) 21695

[8] R. Lv, S. Gai, Y. Dai, N. Niu, F. He, P. Yang. Highly Uniform Hollow GdF_3 Spheres: Controllable Synthesis, Tuned Luminescence, and Drug-Release Properties. ACS Appl. Mater. Interfaces. 5 (2013) 10806−10818

[9] X. Yang, Y. Zhang, L. Xu, Z. Zhai, M. Li, M. Li, X. Liua, W. Hou. Surfactant-free sacrificial template synthesis of submicrometer-sized $YVO_4:Eu^{3+}$ hierarchical hollow spheres with tunable textual parameters and luminescent properties. Dalton Trans. 42 (2013) 3986–3993

[10] J. Y. Tang, H. Zhong, L.Y. Hao, X. Xu, Synthesis of the uniform hollow spherical $Sr_2SiO_4:Eu^{2+}$ phosphors via an h-BN protective method. Opt. Mater. 35 (2013) 2618–2623

[11] X. Kang, D. Yang, P. Ma, Y. Dai, M. Shang, D. Geng, Z. Cheng, J. Lin. Fabrication of Hollow and Porous Structured $GdVO_4:Dy^{3+}$ Nanospheres as Anticancer Drug Carrier and MRI Contrast Agent. Langmuir 29 (2013) 1286−1294

[12] X. Kang, D. Yang, Y. Dai, M. Shang, Z. Cheng, X. Zhang, H. Lian, P. Ma, J. Lin. Poly(acrylic acid) modified lanthanide-doped $GdVO_4$ hollow spheres for up-conversion cell imaging, MRI and pH-dependent drug release. Nanoscale, 5 (2013) 253–261

[13] S. Ye, F. Xiao, Y.X. Pan, Y.Y. Ma, Q.Y. Zhang. Phosphors in phosphor-converted white light-emitting diodes: Recent advances in materials, techniques and properties. Mater. Sci, Eng. R-Rep. 71 (2010) 1–34

[14] R.P. Rao, D.J. Devine. RE-Activated Lanthanide Phosphate Phosphors for PDP Applications. J. Lumin. 87-89 (2000) 1260-1263

[15] T. Liu, Z.M. Yang, S.H. Xu. 3-Dimensional heat analysis in short-length $Er^{3+/}Yb^{3+}$ co-doped phosphate fiber laser with up-conversion. Opt. Express. 17 (2009) 235–247.

[16] Y. Liu, D. Tu, H. Zhu, E. Ma, X. Chen. Lanthanide-doped luminescent nano-bioprobes: from fundamentals to biodetection. Nanoscale, 5 (2013) 1369-1384

[17] Z. Gu, L. Yan, G. Tian, S. Li, Z. Chai, Y. Zhao. Recent Advances in Design and Fabrication of Upconversion Nanoparticles and Their Safe Theranostic Applications. Adv. Mater. 25 (2013) 3758-3779

[18] L. Gu, J.H. Park, K. H. Duong, E. Ruoslahti, M.J. Sailor. Magnetic Luminescent Porous Silicon Microparticles for Localized Delivery of Molecular Drug Payloads. Small 6 (2010) 2546–2552

[19] J. W. Stouwdam, F. C. J. M. van Veggel. Nano Lett. 2002; 2: 733-737 (b) R. Yan, Y. Li, Down/Up Conversion in Ln^{3+}-Doped YF_3 Nanocrystals. Adv. Funct. Mater. 15 (2005) 763-770

[20] M. Ding, C. Lu, L. Cao, Y. Ni, Z. Xu, Synthesis and upconversion luminescence in highly crystalline YOF:$Yb^{3+/}Er^{3+}$ and Yb^{3+}/Tm^{3+} microboxes. Opt. Mater. 35 (2013) 1283–1287

[21] H. Wang, R. Wang, X. Sun, R. Yan, Y. Li. Synthesis of red-luminescent Eu^{3+}-doped lanthanides compounds hollow spheres. Mater. Res. Bull. 40 (2005) 911–919

[22] A. Khanal, Y. Inoue, M. Yada, K Nakashima,. Synthesis of Silica Hollow Nanoparticles Templated by Polymeric Micelle with Core−Shell−Corona Structure. J. Am. Chem. Soc. 129 (2007) 1534−1535

[23] F. Q. Tang, L.L. Li, D. Chen. Mesoporous Silica Nanoparticles: Synthesis, Biocompatibility and Drug Delivery. Adv. Mater. 24 (2012) 1504−1534

[24] G. Tian, Z. J. Gu, X. X. Liu, L. J. Zhou, W. Y. Yin, L. Yan, S. Jin, W. L. Ren, G. M. Xing, S. J. Li, Y. L. Zhao. Facile Fabrication of Rare-Earth-Doped Gd_2O_3 Hollow Spheres with Upconversion Luminescence, Magnetic Resonance, and Drug Delivery Properties. J. Phys. Chem. C, 115 (2011) 23790−23796

[25] G.L. Messing, S.C. Zhang, G.V. Jayanthi, Ceramic powder synthesis by spray pyrolysis, J. Am. Ceram. Soc. 76 (1993) 2707-2726.

[26] M. Eslamian, M. Ahmed, N. Ashgriz. Modeling of Nano-particle Formation during Spray Pyrolysis Nanotechnology. 17 (2006) 1674-1685

[27] M. Mosiadz, K.L. Juda, S.C. Hopkins. An in-depth in situ IR study of the thermal decomposition of yttrium trifluoroacetate hydrate. J.Therm. Anal. Calorim. 107 (2012) 681-691

[28] F. Hund, Yttrium oxyfluorid. Z. Anorg. Allg. Chem., 265 (1951) 62-66

[29] E. Lopez-Navarrete, M. Ocaña. A simple procedure for the preparation of Cr-doped tin sphene pigments in the absence of fluxes. J Eur Ceram Soc 22 (2002) 353-359

[30] M. Ocaña, J.P. Espinós, J.B. Carda. Synthesis, through pyrolysis of aerosols, of $YIn_{1-x}Mn_xO_3$ blue pigments and their efficiency for colouring glazes. Dyes Pigments 91 (2011) 501-507

[31] T. Wen, W. Luo, Y. Wang, M. Zhang, Y. Guo, J. Yuan, J. Ju, Y. Wang, F. Liao, B. Yang. Multicolour and up-conversion fluorescence of lanthanide doped Vernier phase yttrium oxyfluoride nanocrystals. J. Mater. Chem. C, 1 (2013) 1995-2001

[32] N. Rakov, R.B. Guimaraes, W. Lozano, G. S. Maciel. Structural and spectroscopic analyses of europium doped yttrium oxyfluoride powders prepared by combustion synthesis. J. Appl. Phys. 114 (2013) 043517 (1-7)

[33] Y. Zhang, X. Li, D. Geng, M. Shang, H. Lian, Z. Cheng, J. Lin. YOF nano/micro-crystals: morphology controlled hydrothermal synthesis and luminescence properties. CrysEngComm. 16 (2014) 2196-2204

[34] S. Rodriguez-Liviano, F. J. Aparicio , T.C. Rojas, A.B. Hungría, L.E. Chinchilla, M. Ocaña. Microwave-Assisted Synthesis and Luminescence of Mesoporous RE-

Doped YPO_4 (RE = Eu, Ce, Tb, and Ce + Tb) Nanophosphors with Lenticular Shape. Cryst. Growth & Des. 12 (2012) 635-645

[35] M.H.V. Werts, R.T.F. Jukes, J.W. Verhoeven. "The emission spectrum and the radiative lifetime of Eu^{3+} in luminescent lanthanide complexes" Phys. Chem. Chem. Phys. 4 (2002) 1542-1548

[36] D. Hreniak, W. Strek, J. Amani, Y. Guyot, G. Boulon, C. Goutaudier, R. Pazik. "The size-effect on luminescence properties of $BaTiO_3$:Eu^{3+} nanocrystallites prepared by the sol-gel method" J. Alloys Compd. 380 (2004) 348-351

[37] W.T. Carnall, H. M. Crosswhite, H. Crosswhite. "Energy level structure and transition probabilities in the spectra of the trivalent lanthanides in LaF_3," Argonne National Lab., IL (USA) Technical Report (1978) doi: 10.2172/6417825

[38] S. Jie, S. Ling-Dong, Y. Chun-Hua, "Luminescent rare earth nanomaterials for bioprobe applications" Dalton Trans., 42 (2008) 5687-5697

[39] Z. Li, Y. Zhang, S. Jiang. "Multicolor Core/shell-structured upconversion Fluorescent nanoparticles" Adv. Mat., 20 (2008) 4765-4769

[40] M. Haase, H. Schäfer. "Upconverting nanoparticles" Angew. Chem. 50 (2011) 5808-5829

[41] D.K. Chatterjee, M. K. Gnanasammandhan, Y. Zhang."Small upconverting Fluorescent nanoparticles for biomedical applications" Small, 24 (2010) 2781-2795

[42] E. Cantelar, F. Cusso. "Competitive up-conversion mechanisms in Er^{3+}/Yb^{3+} co-doped $LiNbO_3$" J. Lumin. 102–103 (2003) 525–531

[43] G. Yi, , Y. Peng, Z. Gao. Strong Red-Emitting near-Infrared-to-Visible Upconversion Fluorescent Nanoparticles. Chem Mater. 23 (2011) 2729-2734

[44] H. Wang, W. Lu, T. Zeng, Z. Yi, L. Rao, H. Liu, S. Zeng. Multi-functional $NaErF_4$:Yb nanorods: enhanced red upconversion emission, in vitro cell, in vivo X-ray, and T2-weighted magnetic resonance imaging. Nanoscale, 6 (2014) 2855-2860

[45] Z. Li, L. Zheng, L. Zhang, L. Xiong. "Synthesis, characterization and upconversion emission properties of the nanocrystals of Yb^{3+}/Er^{3+}-codoped YF_3-YOF-Y_2O_3 system" J. Lumin., 126 (2007) 481-486

[46] M. Marin-Dobrincic, E. Cantelar, F. Cusso. "Temporal dynamics of IR-to-visible up-conversion in $LiNbO_3$:Er^{3+}/Yb^{3+}: a path to phosphors with tunable chromaticity" Opt. Mater. Express 2 (2012) 1529–1537

[47] L. Tao, W. Xu, Y.S. Zhu, L. Xu, H.C. Zhu, Y.X. Liu, S. Xu, P.W. Zhou, H.W. Song. "Modulation of upconversion luminescence in Er^{3+}, Yb^{3+}-codoped lanthanide oxyfluoride (YOF, GdOF, LaOF) inverse opals" J. Mater. Chem. C, 2 (2014) 4186-4195

[48] H. Schafer, P. Ptacek, H. Eickmeier, M. Haase. "Synthesis of Hexagonal Yb^{3+},Er^{3+}-Doped $NaYF_4$ Nanocrystals

Figure Captions

Figure 1. Schematic diagram of the apparatus used to synthesize the hollow spherical Ln-doped YOF particles.

Figure 2. SEM (top) and TEM (bottom) images of the Eu:YOF particles synthesised by spray pyrolysis according to procedure described in the experimental section

Figure 3. Volumetric size distribution obtained from laser diffraction for the sample shown in figure 2.

Figure 4. a) HAADF-STEM image of a spherical particle, b) Intensity profile of the HAADF signal along the scanned line; and c) Y, Eu and F elemental distribution along the scanned line.

Figure 5. N_2-isothem obtained for the sample shown in figure 2

Figure 6. FTIR spectrum recorded for the samples shown in figure 2

Figure 7. Top: X-ray diffraction patterns recorded for the Eu:YOF samples having different Eu content and ICDD file for cubic YOF. Bottom: Evolution of the unit cell volume determined for the Eu-doped samples

Figure 8. X-ray diffraction patterns recorded for the Er.Yb codped YOF sample. The ICCD file for cubic YOF is also included.

Figure 9. Emission spectra (λ_{em}= 393 nm) of the Eu:YOF samples with different Eu content.

Figure 10. Normalized temporal decays of the $^5D_0$ level, measured at λ_{em} = 612 nm ($^5D_0 \rightarrow {}^7F_2$ transition), for different Eu concentrations. The decays follow a mono-exponential time dependence with lifetimes (τ) that remain constant for Eu concentrations up to 12 % and becomes shortened for 16 % Eu content.

Figure 11. Excitation spectrum (λ_{em}= 612 nm) of the Eu:YOF sample containing a 12% of Eu (top) and emission spectra recorded for the same sample using different excitation

wavelengths (bottom). Inset: Photograph of the Eu:YOF sample containing a 12% of Eu, taken under UV (250 nm) illumination

Figure 12. Schematic energy levels of Yb^{3+} and Er^{3+} ions indicating the different energy transfer processes (ET-1-3) occurring after Yb^{3+} excitation (λ_{ex} ~ 980 nm), populating different Er^{3+} excited states and giving rise to different emissions in the near infrared and visible spectral ranges.

Figure 13. (a) IR- and (b) up-converted luminescence of Er/Yb: YOF, after Yb^{3+} excitation (λ_{ex} ~ 980 nm). The corresponding electronic transitions for the different emission bands are indicated in the figure. The inset shows a photograph of the up-conversion emission of the powders exhibiting a bright red colour.

Figure 14 Double logarithmic plot of the power dependence of the up-converted emissions. Both (red and green) emissions exhibit a quadratic dependence (slope 1.9 and 2.0).

Table 1. Nominal and experimental Ln/Y mol ratio (Ln = Eu, Er and Yb), unit cell parameter and unit cell volume for the Eu doped and Er,Yb codoped samples. The lifetime (τ) and quantum yield (QY) values measured for the Eu-doped samples (λ_{em} = 612 nm) are also included. Errors are given in parenthesis.

Eu (mol%) Nom.	**Eu (mol%) Exper.**	**Er (mol%) Nom.**	**Er (mol%) Exper.**	**Yb (mol%) Nom.**	Yb (mol%) Exper.	**a (Å)**	**V (Å^3)**	**τ (ms)**	**QY (%)**
2.0	2.0					5,4181(9)	159,0530	2.0± 0.2	91
4.0	4.1					5,4204(9)	159,2546	2.1± 0.2	95
8.0	8.2					5,4251(8)	159,6700	2.0± 0.2	91
12.0	12.3					5.4310 (7)	160,1945	2.0± 0.2	91
16.0	16.5					5,4316(4)	160,2427	1.4± 0.2	64
		2.0	2.1	10.0	9.7	5,4100(10)	158,3508		

Graphical Abstract (for review)

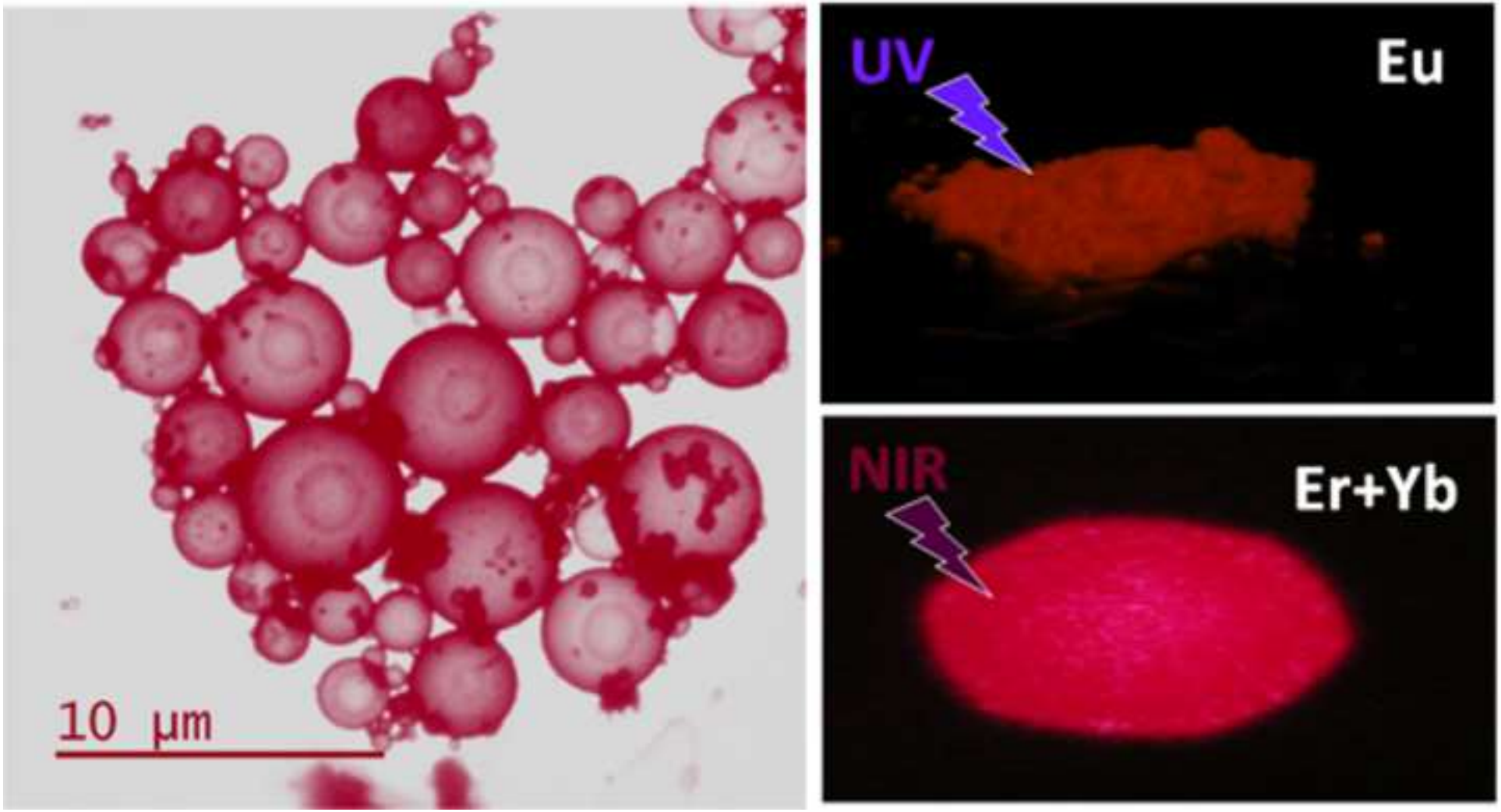

Highlights

- Hollow lanthanide doped YOF spheres have been synthesised through a template-free procedure
- Strong red emissions are observed for Eu-doped spheres under UV illumination
- Concentration quenching of luminescence takes place in the spheres at very high Eu doping levels
- Bright red emission is observed for Er,Yb codoped spheres, making this matrix advantageous for biomedical imaging

Figure

Click here to download high resolution image

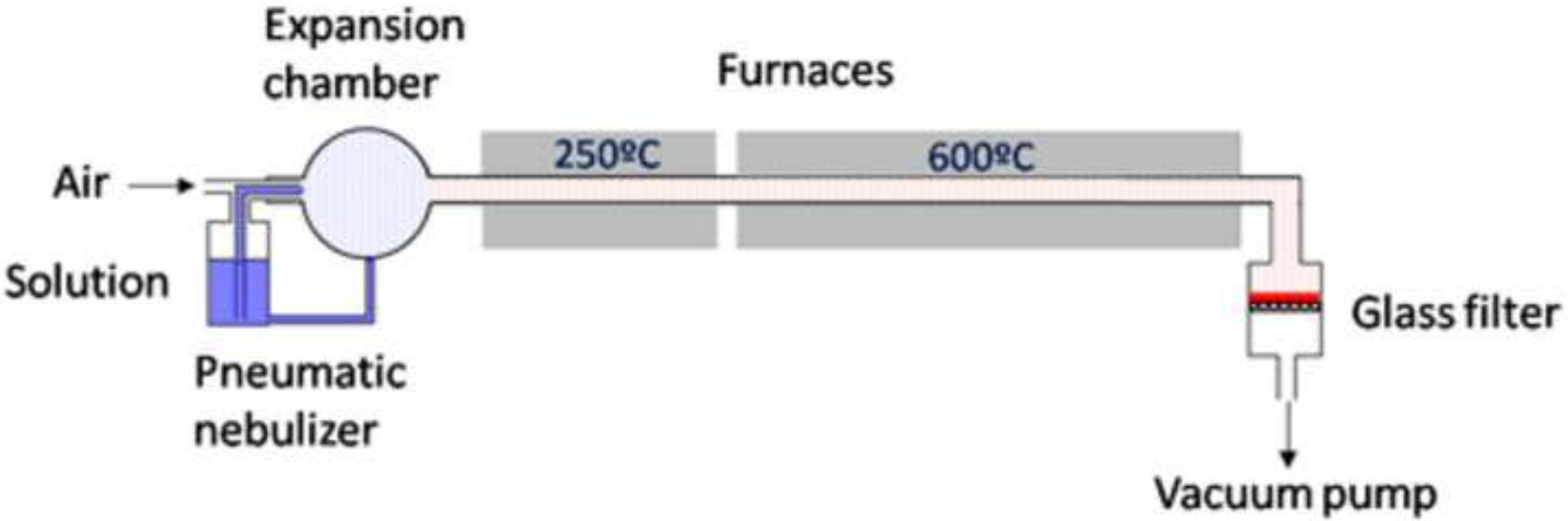

Figure

Click here to download high resolution image

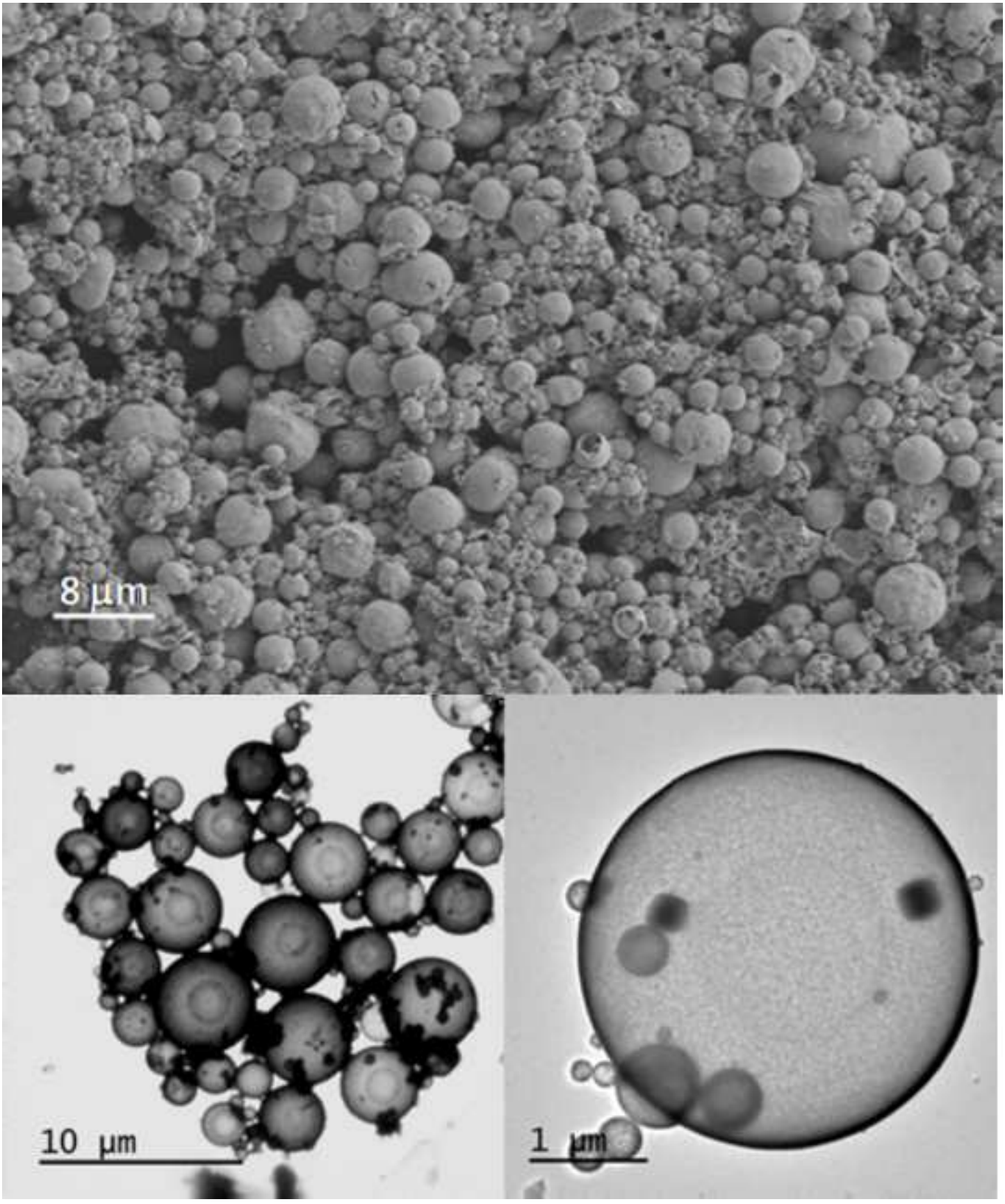

Figure 3

Click here to download high resolution image

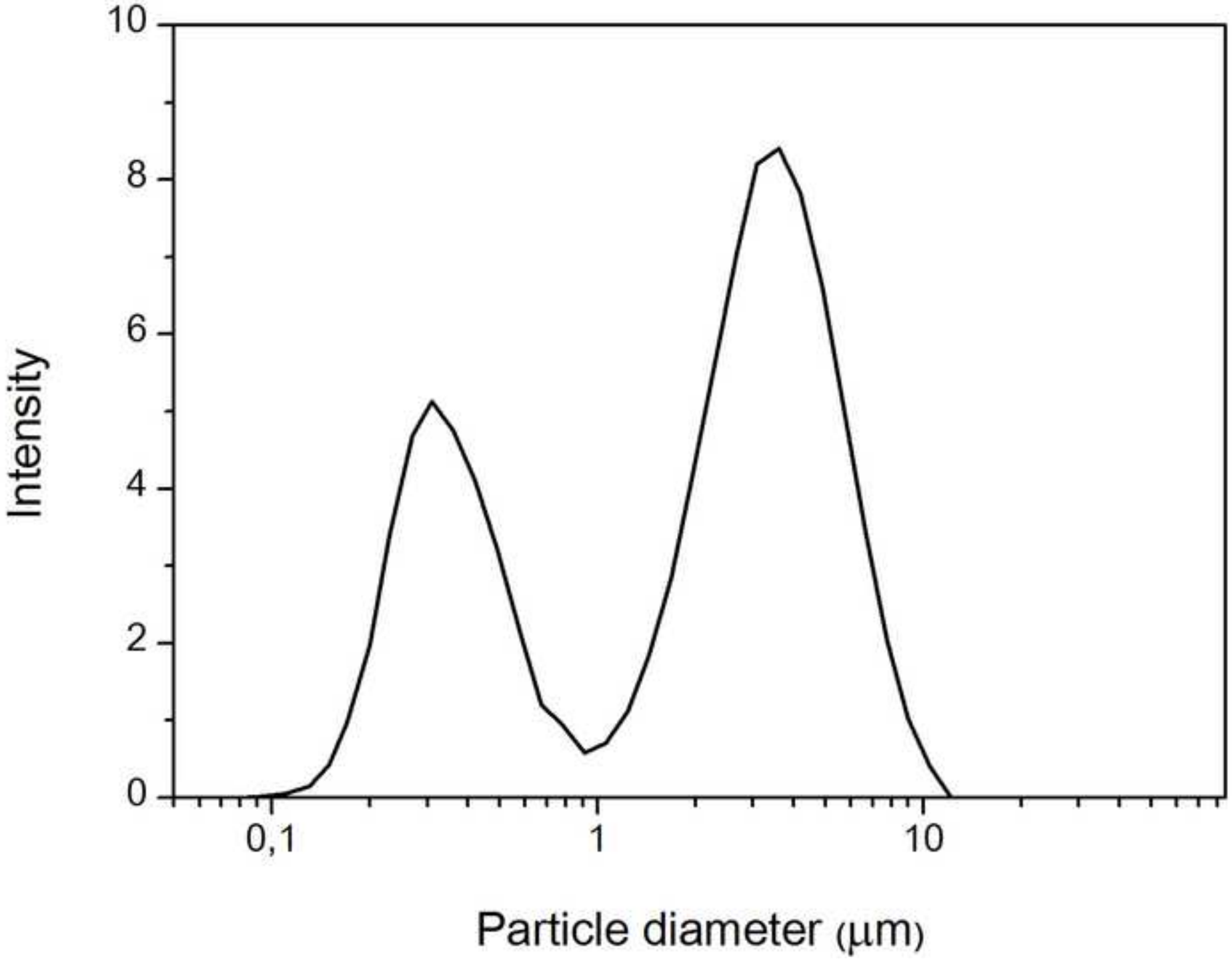

Figure 4

Click here to download high resolution image

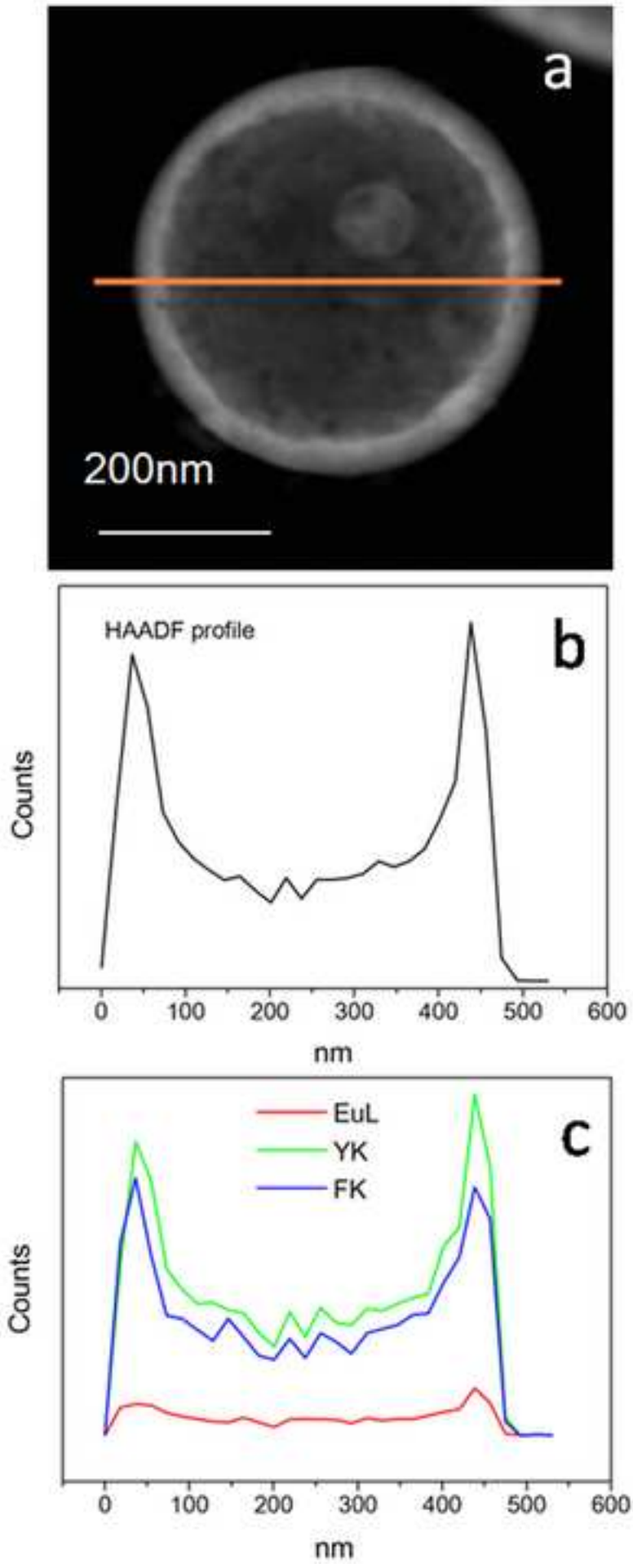

Figure 5

Click here to download high resolution image

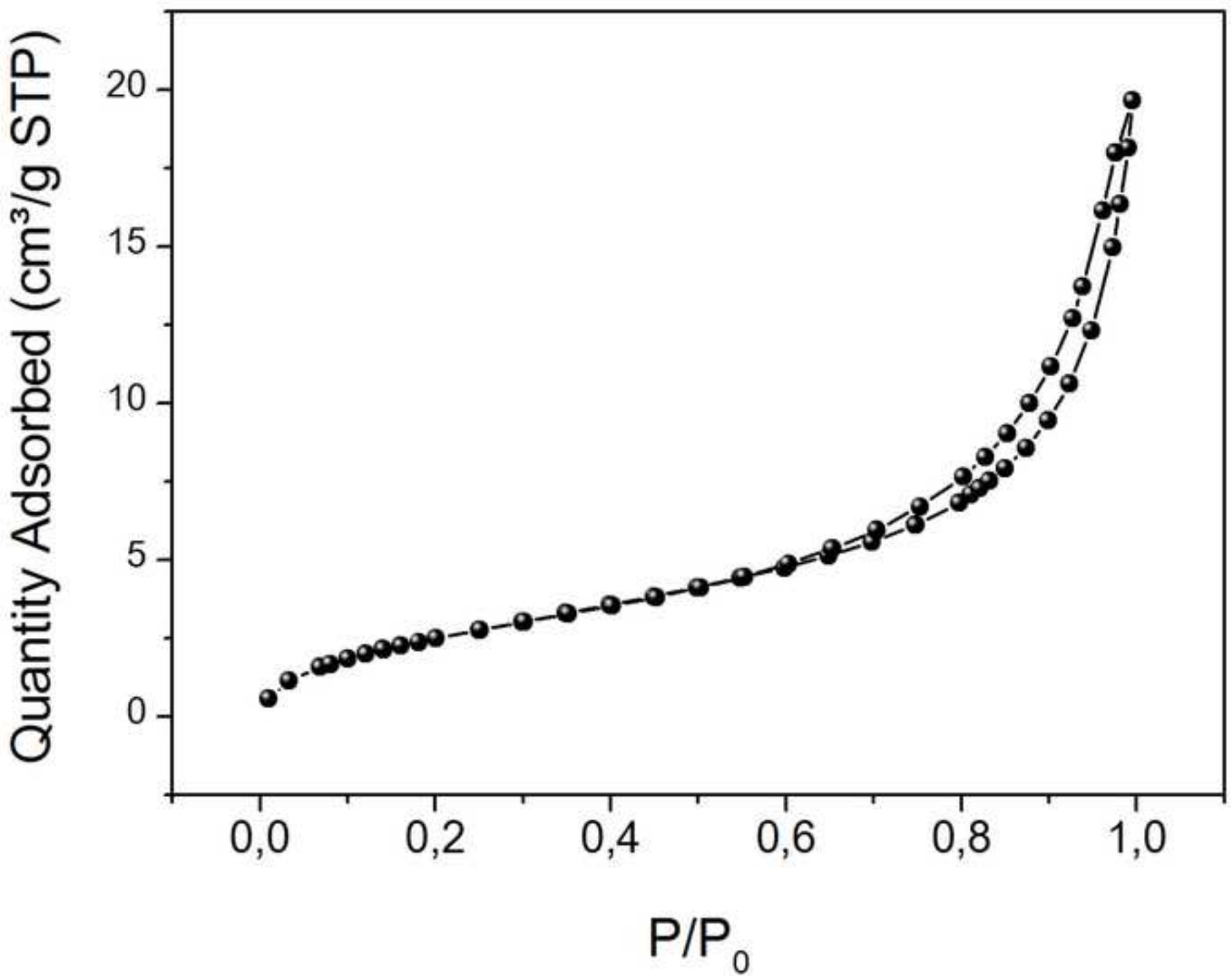

Figure 6

Click here to download high resolution image

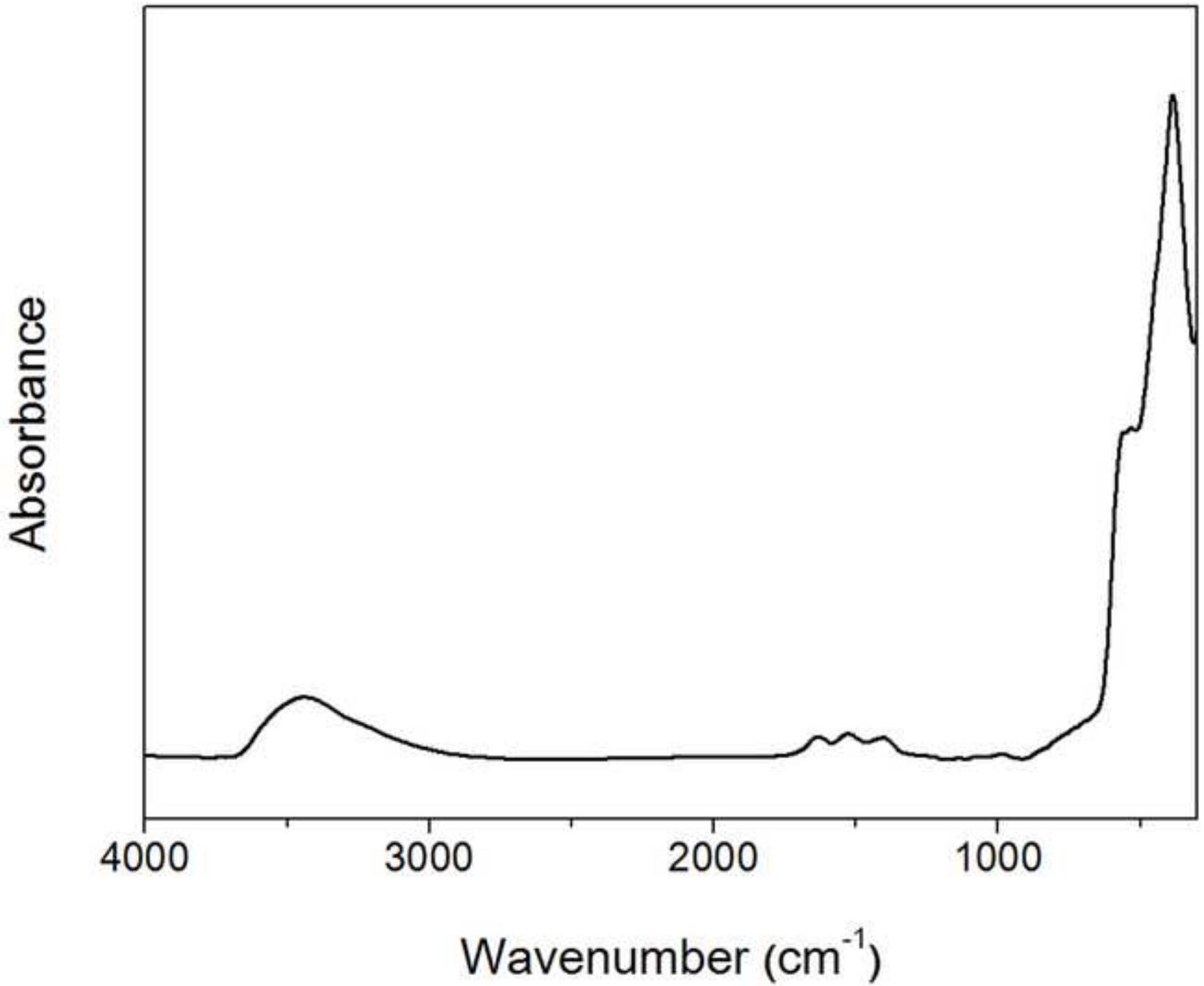

Figure 7

Click here to download high resolution image

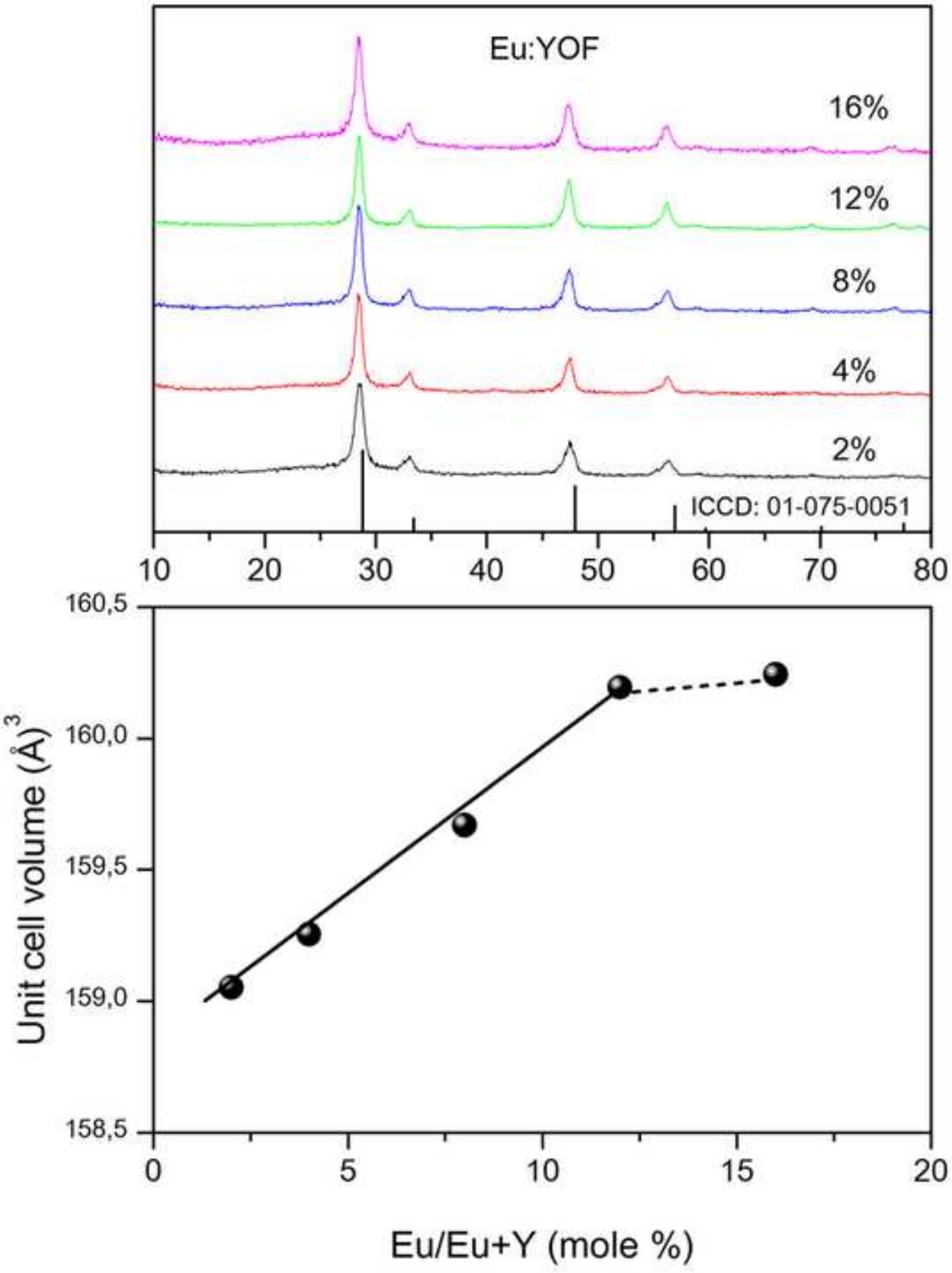

Figure 8

Click here to download high resolution image

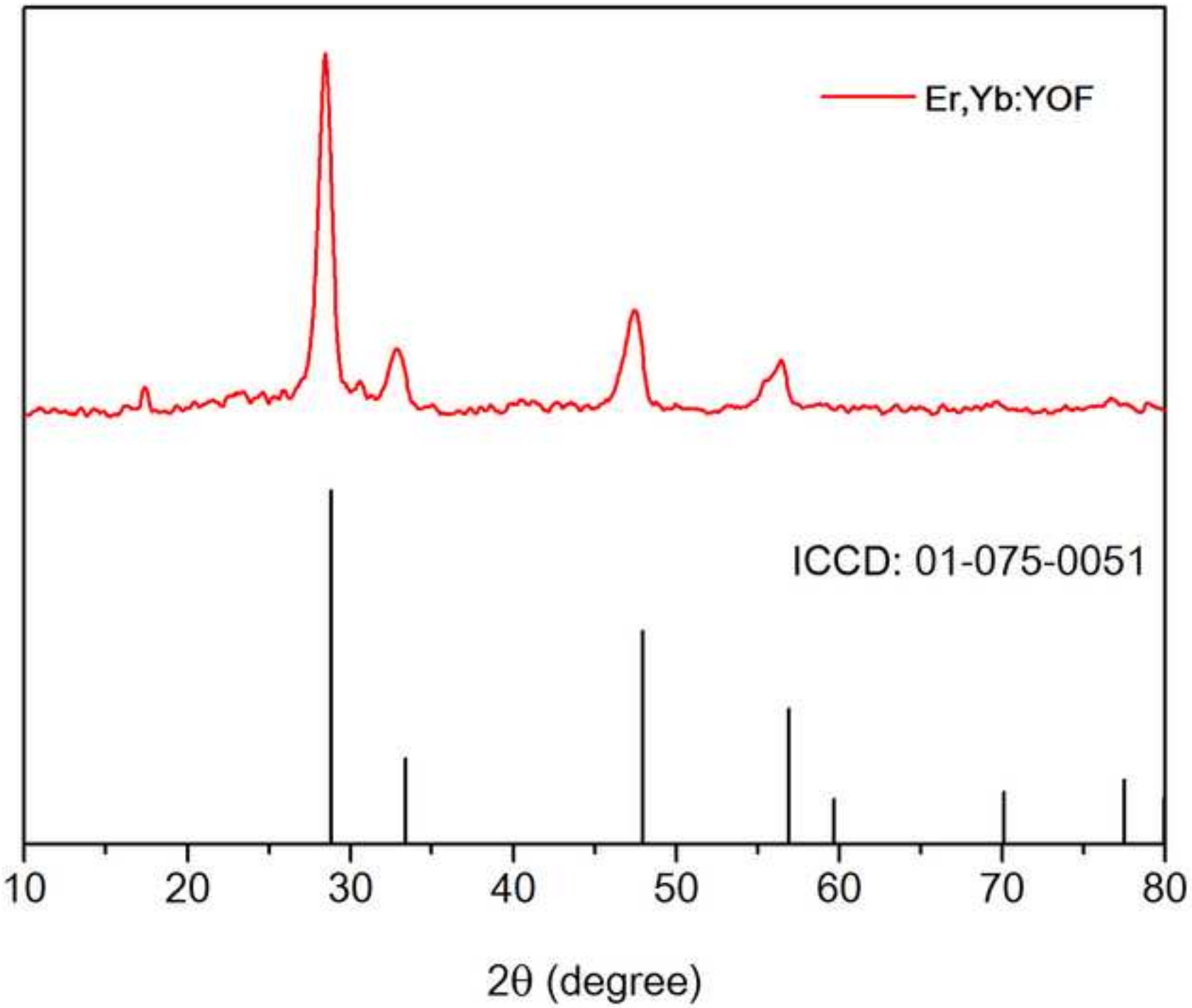

Figure 9

Click here to download high resolution image

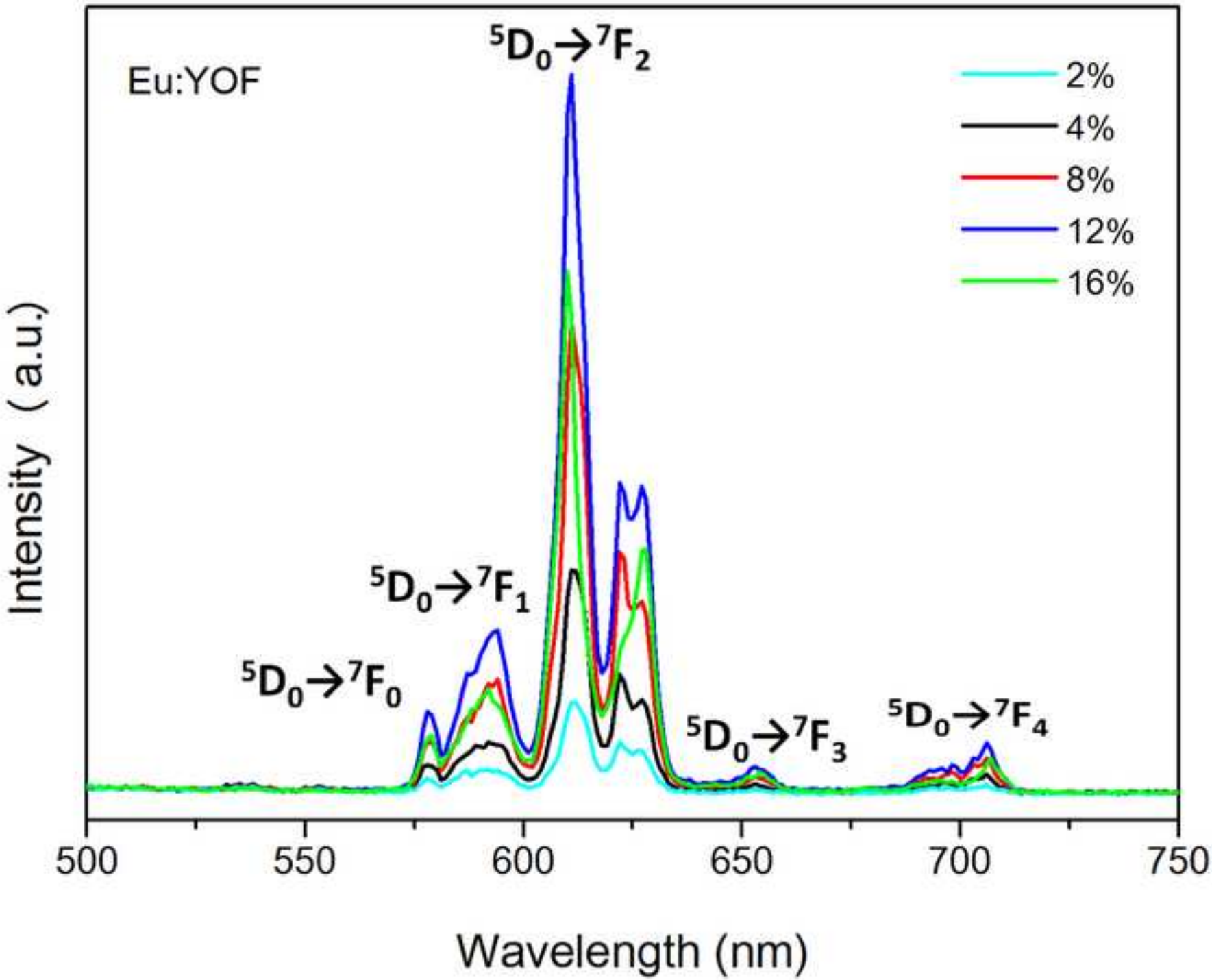

Figure 10

Click here to download high resolution image

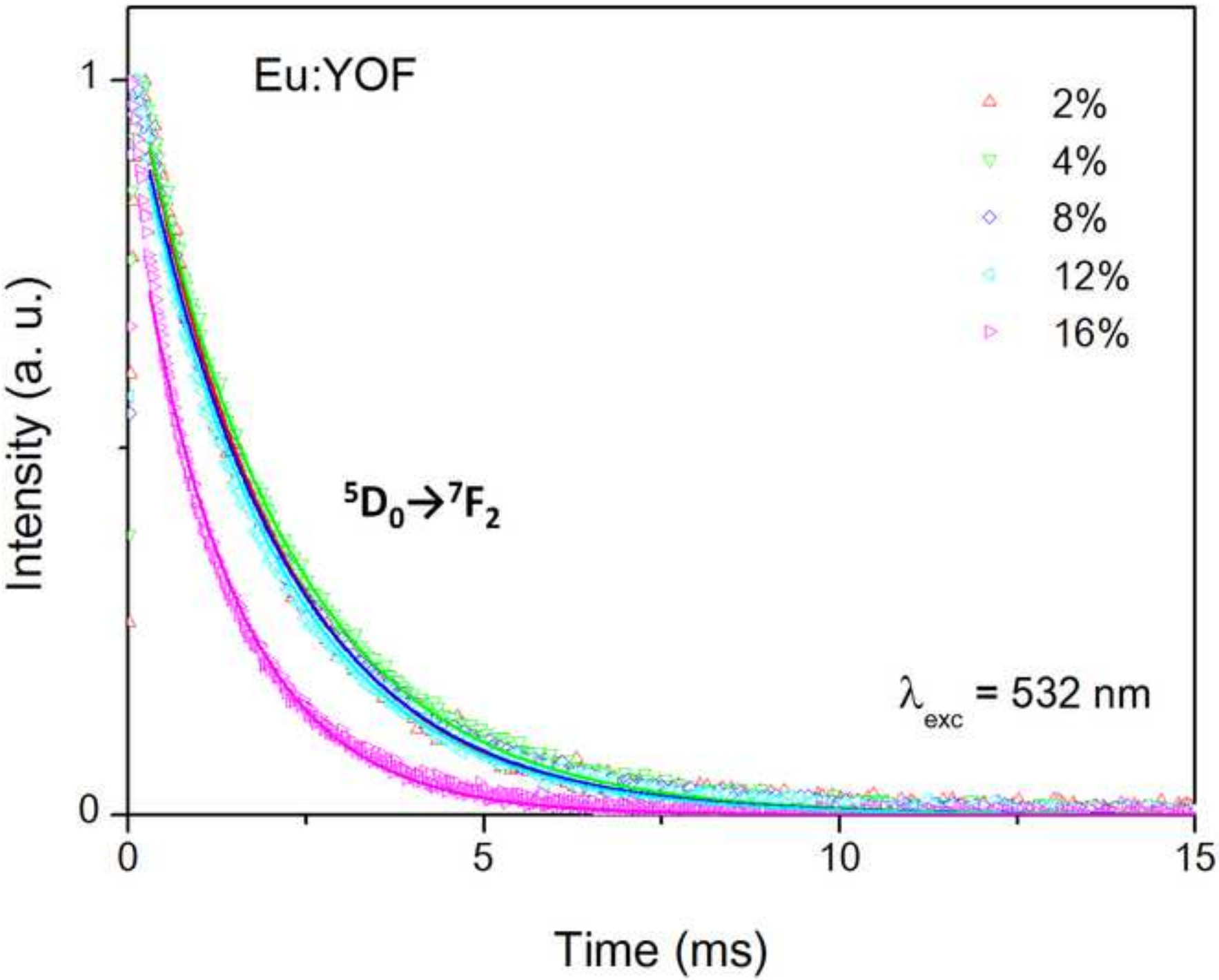

Figure 11

Click here to download high resolution image

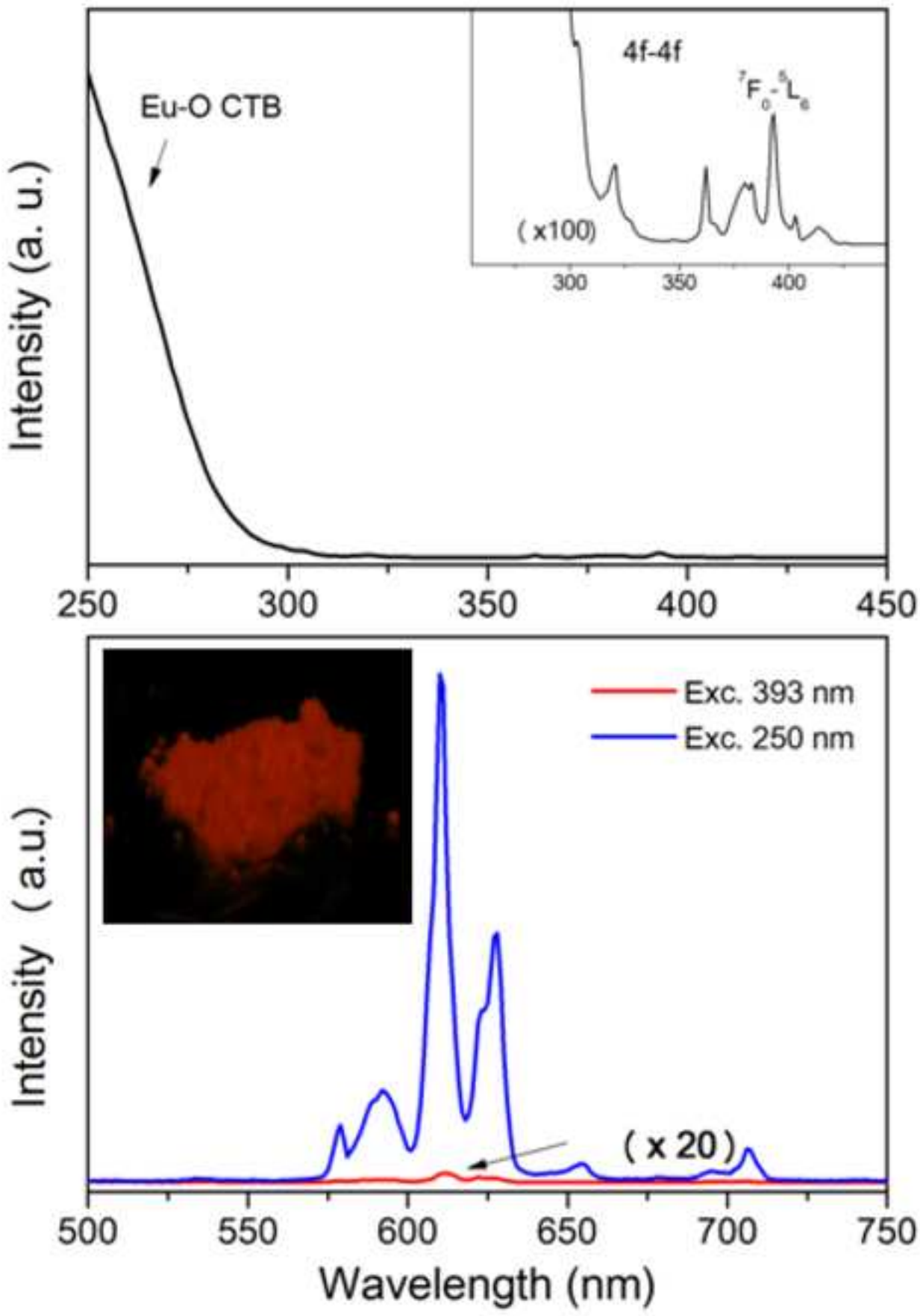

Figure 12

Click here to download high resolution image

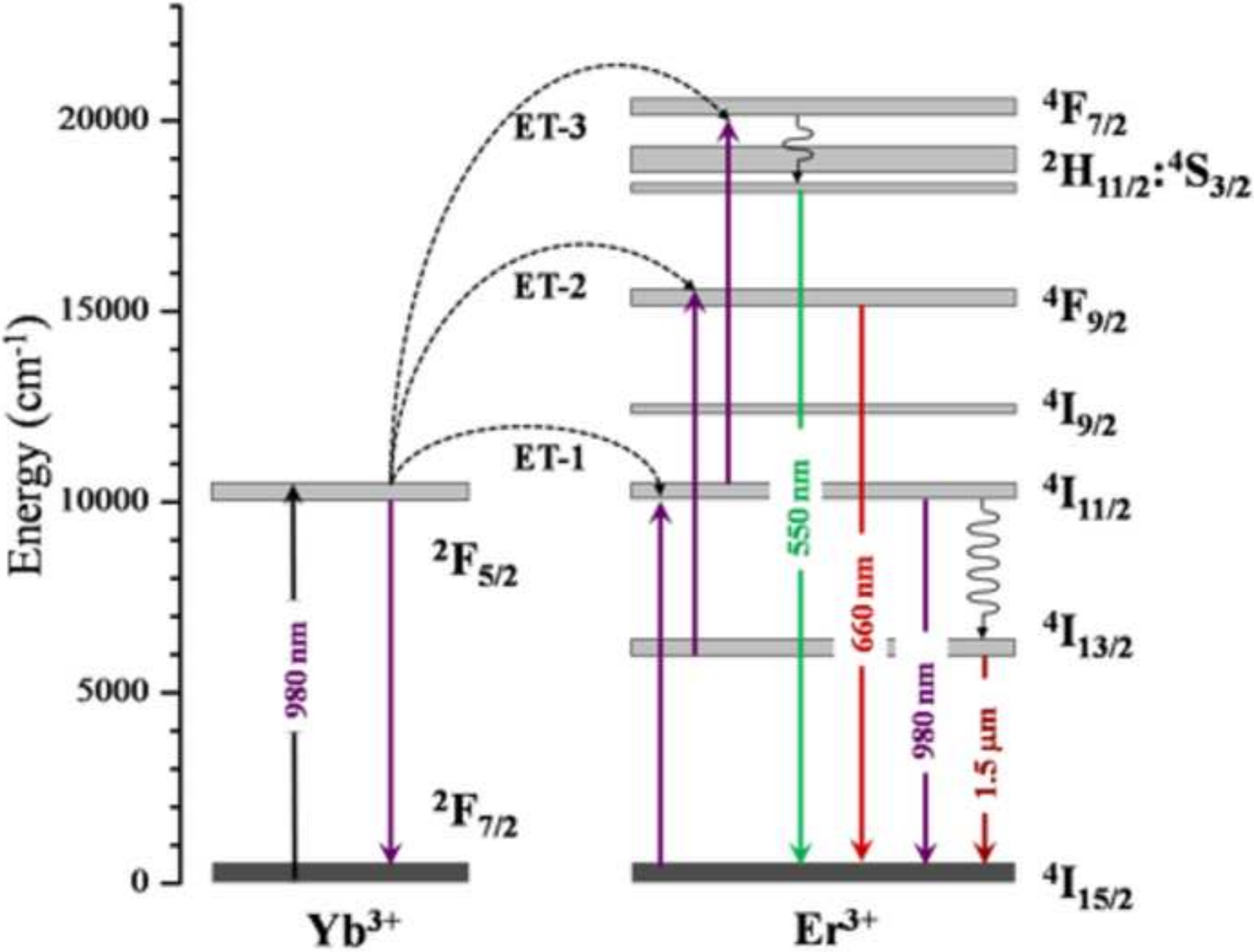

Figure 13

Click here to download high resolution image

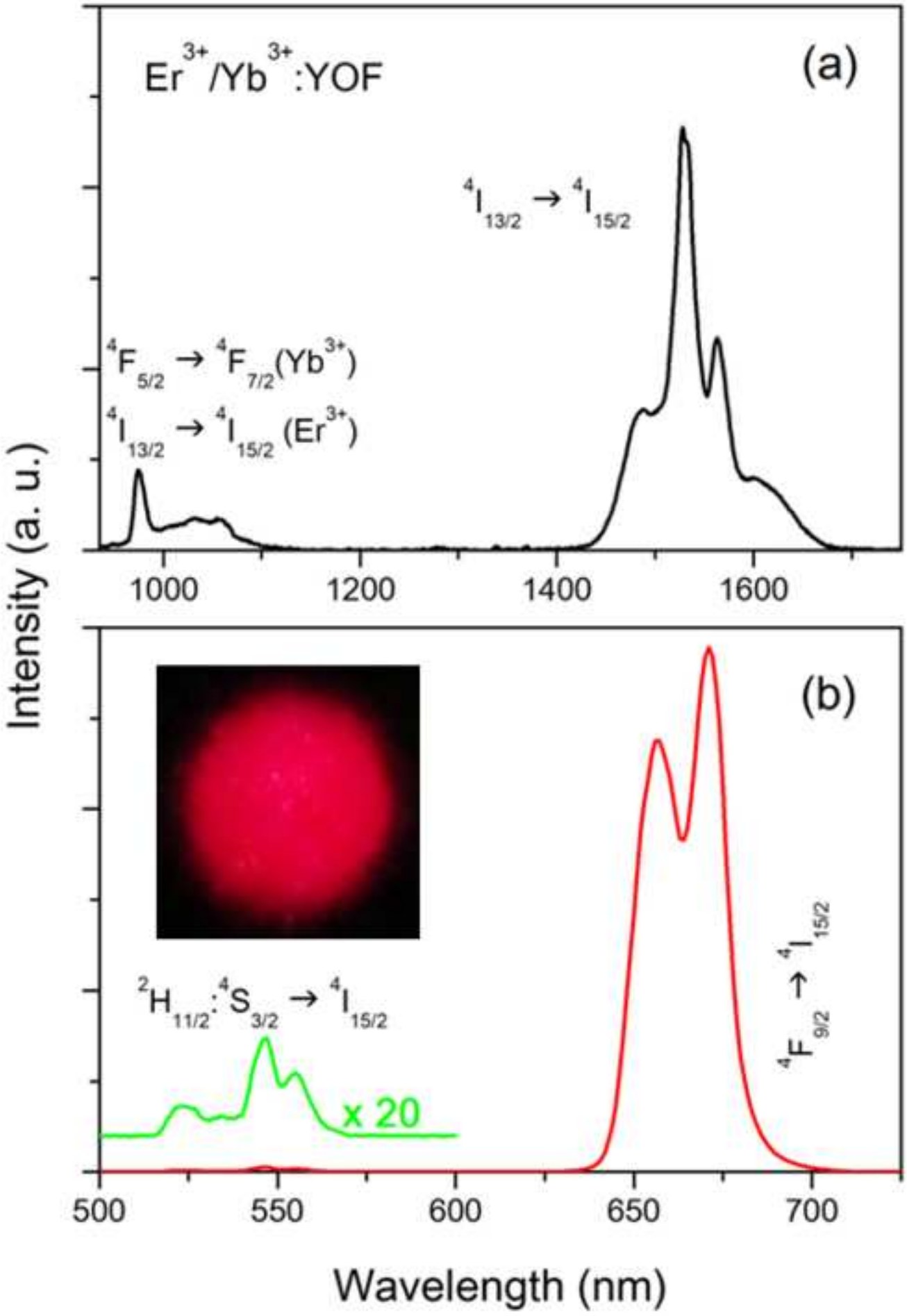

Figure 14

Click here to download high resolution image